Direct numerical simulation of turbulence at lower costs

Verstappen, R.W.C.P.; Veldman, A.E.P.

Published in:
Journal of Engineering Mathematics

Publication date:
1997

Journal of Engineering Mathematics **32:** 143–159, 1997.

Direct numerical simulation of turbulence at lower costs

R.W.C.P. VERSTAPPEN and A.E.P. VELDMAN
Department of Mathematics, University of Groningen, P.O. Box 800, 9700 AV Groningen, The Netherlands
e-mail: verstappen@math.rug.nl

Received 1 November 1996; accepted in revised form 13 February 1997

Abstract. Direct Numerical Simulation (DNS) is the most accurate, but also the most expensive, way of computing turbulent flow. To cut the costs of DNS we consider a family of second-order, explicit one-leg time-integration methods and look for the method with the best linear stability properties. It turns out that this method requires about two times less computational effort than Adams–Bashforth. Next, we discuss a fourth-order finite-volume method that is constructed as the Richardson extrapolate of a classical second-order method. We compare the results of this fourth-order method and the underlying second-order method for a DNS of the flow in a cubical driven cavity at $\mathrm{Re} = 10^4$. Experimental results are available for comparison. For this example, the fourth-order results are clearly superior to the second-order results, whereas their computational effort is about twenty times less. With the improved simulation method, a DNS of a turbulent flow in a cubical lid-driven flow at $\mathrm{Re} = 50,000$ and a DNS of a turbulent flow past a square cylinder at $\mathrm{Re} = 22,000$ are performed.

Key words: DNS, turbulent flow, one-leg method, higher-order finite-volume method, driven-cavity flow, flow past a square cylinder.

1. Introduction

The Navier–Stokes equations form the best model for turbulent flow. Unfortunately, the costs of solving the Navier–Stokes equations at high Reynolds numbers exceed the nowadays available computational resources. Even with the presently fastest numerical methods available for solving the incompressible Navier–Stokes equations in rectangular geometries, a Direct Numerical Simulation (DNS) of a turbulent flow (i.e. a simulation of all dynamically significant scales of motion) at a Reynolds number $\mathrm{Re} = 10^7$ will take about one hundred thousand years on a Gflops machine.

About six orders of magnitude have to be bridged to perform a DNS of a turbulent flow at $\mathrm{Re} = 10^7$. Assuming that both computer hardware and computational algorithms will continue to progress at the rate that they have developed during the past three decades – both have become one and a half order of magnitude faster per decade – it will take roughly two decades to bridge the lacking six orders of magnitude. For this estimate to come true, computers need to become about a thousand times faster and must be supplied with one thousand times as much memory within the next two decades. Within that span of time the numerical algorithms for DNS need to become three orders of magnitude faster, need to run efficiently at the fastest avaliable machines, and need to use three orders of magnitude less memory than today's algorithms do require.

Campaign plans to cut the costs of DNS consist of one or more of the following three issues: (a) introduce larger time steps, (b) use less grid points, and (c) perform fewer iterations, all without deteriorating the numerical solution. In this paper we will focus on item (a) (in Section 3) and on item (b) (in Sections 4 and 5).

In Section 3.1 we will argue that the time step of explicit time integration methods for DNS is not limited by accuracy requirements, but by those of (convective) stability. Thus, there is room for improvement. In Section 3.2 we consider a family of explicit second-order one-leg methods. The 'one' in one-leg refers to the fact that these methods evaluate the right-hand side f of the differential equation $y' = f$ at one point only. For more details on one-leg methods the reader is referred, for instance, to [1].

We look for the explicit second-order one-leg method with the best linear stability properties and compare this method with the (frequently applied) second-order method of Adams and Bashforth. It turns out that there are one-leg methods that are stable for a step size which is roughly twice as large as the largest step for which Adams–Bashforth is stable. Since the work per time step of these one-leg methods is approximately equal to the work per time step of Adams–Bashforth, a cost reduction by a factor of about two is achieved (with regard to Adams–Bashforth). The computational effort of the optimal one-leg method is of about the same level as that of a third-order Runge–Kutta method where the Poisson equation for the pressure is solved only at the final sub-step (see e.g. [2]).

Any grid that is used for a DNS need to be so fine that the smallest length scales in the flow can be resolved accurately. The number of grid points that is needed per smallest length scale depends upon the discretization method that is applied. Lowering this number pays off. For instance, a reduction by a factor of two yields a saving of about one order of magnitude in both computing time and memory (in three spatial dimensions).

In the early days of DNS spectral and pseudo-spectral methods were the prevalent methods. In the search for methods that can handle geometrically complex configurations second-order accurate finite-difference/volume methods became popular. The questioning of the cost-effectiveness of these methods gave birth to higher-order finite-difference methods, often applied in combination with (pseudo-)spectral methods in homogeneous directions. Rai and Moin [3] introduced a fifth-order upwind-biased method for the convective terms and a sixth-order central method for the viscous terms; Fasel [4] used a velocity/vorticity formulation with fourth-order finite differences; Joslin et al. [5] have applied a fourth-order compact method for the momentum equations; Liu et al. [6] have developed a transformation of a standard fourth-order difference scheme in computational space into physical space. Kravchenko et al. [7] have applied a Galerkin method with B-spline basis functions for numerical simulations of turbulent channel flows.

This brief enumeration of higher-order DNS methods shows that there are several ways of making them. Although Richardson extrapolation is a well-known way to increase the order of accuracy of numerical approximations, it has not yet been applied to obtain higher-order DNS methods. In Section 4, we will focus on a fourth-order method that is constructed as the Richardson extrapolate of a classical second-order finite-volume method. In Section 5 the results of the fourth-order accurate finite-volume method and the underlying second-order method are compared for a direct numerical simulation of the flow in a cubical driven cavity at $\mathrm{Re} = 10,000$. Experimental results are available for comparison. For this example, the fourth-order results are clearly superior to the second-order results, whereas their computational effort is about twenty times less.

With the improved simulation method, a DNS of a turbulent flow in a cubical lid-driven flow at $\mathrm{Re} = 50,000$ and a DNS of a turbulent flow past a square cylinder at $\mathrm{Re} = 22,000$ have been performed. Results of these two simulations are presented in Sections 6 and 7 respectively. The flow past a square cylinder at $\mathrm{Re} = 22,000$ (at zero angle of attack) has served as a test

case for two LES workshops. Experimental data is also available for comparison. A summary of the results presented at the workshops can be found in [8] and [9].

2. Incompressible turbulent flows

The conservation laws for momentum and mass of an incompressible fluid read

$$\frac{\partial}{\partial t}\int_\Omega \mathbf{u}\,\mathrm{d}\Omega - \oint_{\partial\Omega} \mathbf{f}(\mathbf{u})\,\mathbf{n}\,\mathrm{d}s + \oint_{\partial\Omega} p\,\mathbf{n}\,\mathrm{d}s = \mathbf{0}, \tag{1}$$

$$\oint_S \mathbf{u}\cdot\mathbf{n}\,\mathrm{d}s = 0, \tag{2}$$

where Ω is an arbitrary volume with boundary $\partial\Omega$; S is an arbitrary surface; $\mathbf{n}$ denotes the unit normal vector on the surface of integration. The vector $\mathbf{u}$ denotes the velocity; the scalar p is the pressure. The flux $\mathbf{f}(\mathbf{u})$ consists of two components, a convective part $\mathbf{f}_c = -\mathbf{u}\mathbf{u}^{\mathbf{T}}$ and a diffusive part $\mathbf{f}_d = \nabla\mathbf{u}/\mathrm{Re}$.

3. Time-integration method

3.1. Stability versus accuracy

In this section, we consider an explicit time-integration method which is stable if the time step satisfies both $2\delta t < \mathrm{Re}\,\delta x^2$ and the CFL-condition $\delta t < \delta x/U_{\max}$. Here, $U_{\max}$ denotes the maximum velocity. These conditions are typical of explicit methods; the constants (here 2 and 1) depend on the method. For the flow in a driven cavity at $\mathrm{Re} = 50,000$ ($\delta x_{\min} = 2{\cdot}5\,10^{-3}$, $U_{\max} = 1$; see Section 6) and the flow past a square cylinder at $\mathrm{Re} = 22,000$ ($\delta x_{\min} = 5\,10^{-3}$, $U_{\max} \approx 1$; Section 7) the time step limitation $\delta x/U_{\max}$ is about two orders of magnitude lower than $\mathrm{Re}\,\delta x^2$. Thus, for the flows under consideration the time step limitation is due to the CFL-condition and not due to the viscous limit.

Next to being stable, an explicit time-integrator used for DNS should also be accurate. In [10] we have compared the CFL-condition with accuracy requirements for flows for which the ratio of the smallest length/time scale in the flow to the largest is given by Kolmogorov's scaling law. For these flows the CFL-condition can be written as

$$n_\mathrm{t} > \frac{U_{\max}}{u_\mathrm{le}}\mathrm{Re}_\mathrm{le}^{0{\cdot}25} n_\mathrm{x},$$

where n_t denotes the number of time steps per smallest time scale and n_x is the number of grid points per smallest length scale. Here, the Reynolds number Re_le is based on the velocity u_le and length scales of the large eddies. The condition above expresses that the CFL-condition forces us to use a time step which is small compared to the smallest (physical) time scale, if the eddies deform at a rate significantly smaller than the maximum velocity $U_{\max}$. The latter holds for many turbulent flows.

So, in conclusion, the time step of explicit time integration methods for DNS is not limited by an accuracy requirement, but by that of (convective) stability.

3.2. An improvement of the Adams–Bashforth scheme

We consider a family of second-order one-leg methods. The second-order (explicit) method of Adams and Bashforth is the multistep twin of a member of this family. The family is

parameterized by α. Our aim is to determine α such that the corresponding method allows for the largest time step, or stated otherwise, possesses the largest region of convective stability.

We denote the velocity and pressure at time $t = n\delta t$ by $\mathbf{u}^n$ and p^n, respectively. Starting from time $t = (n + \alpha - \frac{1}{2})\delta t$, we integrate Equation (1) over one time step δt using the midpoint rule

$$\int_\Omega (\mathbf{u}^{n+\alpha+(1/2)} - \mathbf{u}^{n+\alpha-(1/2)})\,\mathrm{d}\Omega - \delta t \oint_{\partial\Omega} \mathbf{f}(\mathbf{u}^{n+\alpha})\mathbf{n}\,\mathrm{d}s + \delta t \oint_{\partial\Omega} p^{n+\alpha}\mathbf{n}\,\mathrm{d}s = \mathbf{0}. \tag{3}$$

The incompressibility constraint (2) is applied at time level $n + 1$

$$\oint_S \mathbf{u}^{n+1} \cdot \mathbf{n}\,\mathrm{d}s = 0. \tag{4}$$

The velocity and the pressure are defined on integer time levels only. We assume that the velocity and the pressure are known up to and including level n. Then, the velocity $\mathbf{u}^{n+1}$ and the pressure p^{n+1} can be solved from (3) and (4) if the velocities and the pressures at non-integer time levels in Equation (3) are approximated in terms of velocities and pressures at integer levels. We approximate the off-step velocity $\mathbf{u}^{n+\alpha}$ by a linear extrapolation of $\mathbf{u}^n$ and $\mathbf{u}^{n-1}$ and denote the result by

$$\hat{\mathbf{u}} = (1 + \alpha)\mathbf{u}^n - \alpha\mathbf{u}^{n-1}. \tag{5}$$

The off-step pressure $p^{n+\alpha}$ is approximated by

$$\hat{p} = \tfrac{1}{2}(1 + \alpha)p^{n+1} + \tfrac{1}{2}(1 - \alpha)p^{n-1}, \tag{6}$$

i.e. by a linear interpolation between p^{n+1} and p^{n-1}. The off-step velocity $\mathbf{u}^{n+\alpha+(1/2)}$ is approximated by a linear interpolation between $\mathbf{u}^{n+1}$ and $\mathbf{u}^n$. Substituting these off-step approximations in Equation (3), we obtain the one-leg scheme

$$\int_\Omega ((\alpha + \tfrac{1}{2})\mathbf{u}^{n+1} - 2\alpha\mathbf{u}^n + (\alpha - \tfrac{1}{2})\mathbf{u}^{n-1})\,\mathrm{d}\Omega - \delta t \oint_{\partial\Omega} (\mathbf{f}(\hat{\mathbf{u}})\,\mathbf{n} - \hat{p}\,\mathbf{n})\,\mathrm{d}s = \mathbf{0}. \tag{7}$$

This discretization is second-order accurate for all $\alpha \neq -\frac{1}{3}$, and third-order accurate when $\alpha = -\frac{1}{3}$. Its error constant is given by $C_3 = \frac{1}{6}(1 + 3\alpha)$.

The implicit treatment of the pressure (in (6)) and the incompressibility constraint (4) stabilizes the integration method. Therefore, we can discuss the stability without taking the pressure into account. We consider the stability of the one-leg scheme for the (one-dimensional) test problem $u' = f(u)$. For this problem the one-leg scheme reduces to

$$(\alpha + \tfrac{1}{2})u^{n+1} - 2\alpha u^n + (\alpha - \tfrac{1}{2})u^{n-1} = \delta t f((1 + \alpha)u^n - \alpha u^{n-1}). \tag{8}$$

Taking $\alpha = \frac{1}{2}$, we have a one-leg method which is the twin of Adams–Bashforth. According to Adams-Bashforth we ought to take $\frac{3}{2}f(u^n) - \frac{1}{2}f(u^{n-1})$ instead of $f(\frac{3}{2}u^n - \frac{1}{2}u^{n-1})$. One- and two-leg methods are identical if f is linear, and thus have the same region of linear stability. They differ when the right-hand side f is nonlinear. For instance, for $f(u) = \lambda(t)u$ with $\lambda(t) < 0$ and $u^n > 0$ the solution u^{n+1} of Equation (8) is smaller than u^n (for any time step) as it should be, while the solution obtained with the associated multistep method does

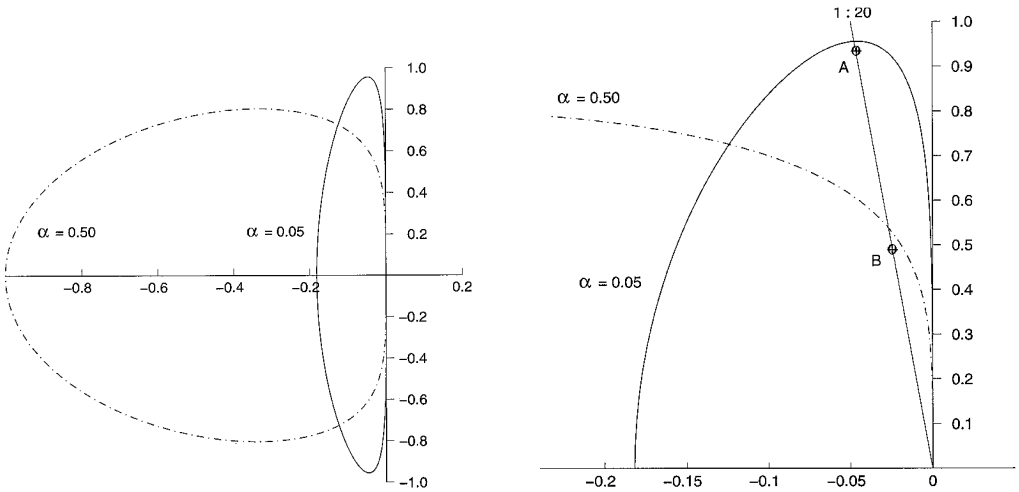

Figure 1. The left picture shows the stability domain of the one-leg method (8) for $\alpha = 0{\cdot}05$ and $\alpha = 0{\cdot}5$. The right picture shows a blow up of the stability domains near the positive imaginary axis.

not satisfy the inequality $u^{n+1} < u^n$ unconditionally. In addition, it is emphasized in [11] that (some) one-leg methods are more reliable than their corresponding multistep methods when used with variable time steps.

For $\alpha = 0$ the leapfrog method is obtained. This method cannot be used to integrate a diffusive flux in time, since it is not stable: the linear stability region of leapfrog consists of all purely imaginary numbers with modulus smaller than or equal to one.

We look for the one-leg method with the best linear stability properties. Figure 1 (left) shows the stability domain of the one-leg method for $\alpha = 0{\cdot}05$ and $\alpha = 0{\cdot}5$ (Adams–Bashforth). The stability domain is pressed against the imaginary axis when α goes to zero. In the limit $\alpha = 0$ the stability domain is equal to the interval $[-i, i]$. In Section 3.1 we concluded that convective stability puts the most severe restriction on the time step. Thus, we look for stability domains which include eigenvalues $\lambda = x + iy$, where the real part x is negative and the absolute value of the imaginary part y is much larger than the absolute value of the real part. Here, 'much' can range from one to two orders of magnitude. For a DNS of a flow in a driven cavity at $\mathrm{Re} = 10^4$ with a grid size $\delta x = 10^{-2}$, and a maximum velocity $U_{\max} = 1$, for example, $|x| : |y|$ is of the order of $1 : 100$.

Under these conditions, the one-leg method with $\alpha = 0{\cdot}05$ outperforms Adams–Bashforth. Figure 1 (right) shows a blow up of the stability domains of both methods near the positive imaginary axis. The points denoted by A and B lie on the line $|x| : |y| = 1 : 20$. The point A lies close to the boundary of the stability domain for $\alpha = 0{\cdot}05$; B lies near to the boundary of the stability domain for $\alpha = 0{\cdot}5$. A lies approximately two times as far from the origin as B. Thus, the time step of the one-leg method with $\alpha = 0{\cdot}05$ can be enlarged by a factor of two compared to Adams–Bashforth. For $|x| : |y| = 1 : 10$ this factor is about 1·5; for $|x| : |y| = 1 : 100$ it is approximately 2·5. We have carried out a number of numerical test calculations of the (2D) flow in a driven cavity at $\mathrm{Re} = 10^3 - 10^5$. The results demonstrate that the one-leg method with $\alpha = 0{\cdot}05$ requires indeed about two times less computational effort than the Adams–Bashforth method, whereas the accuracy is just as good.

To implement the one-leg scheme (8) using minimal storage, we write Equation (8) as

$$(\alpha+\tfrac{1}{2})\delta u^{n+(1/2)} - (\alpha-\tfrac{1}{2})\delta u^{n-(1/2)} = \delta t f(u^n + \alpha\delta u^{n-(1/2)}), \tag{9}$$

where

$$\delta u^{n+(1/2)} = u^{n+1} - u^n.$$

We need to store just two quantities, namely $a = \delta u^{n-(1/2)}$ and $b = u^n$. Indeed, the computation of one step can be implemented as follows: $(\alpha+\frac{1}{2})a := (\alpha-\frac{1}{2})a + \delta t f(b+\alpha a)$ and $b := a + b$. Finally, it may be noted that the computation of $\mathbf{u}^{n+1}$ and p^{n+1} from (6) and (4) is divided into two steps. In the first step, the pressure at time $(n+\alpha)\delta t$ is not approximated implicitly as in (6), but explicitly. That is, the off-step pressure $p^{n+\alpha}$ is approximated (like the off-step velocity) by $\breve{p} = (1+\alpha)p^n - \alpha p^{n-1}$. The resulting auxiliary velocity is denoted by $\breve{\mathbf{u}}$

$$\int_\Omega ((\alpha+\tfrac{1}{2})\breve{\mathbf{u}} - 2\alpha\mathbf{u}^n + (\alpha-\tfrac{1}{2})\mathbf{u}^{n-1})\,\mathrm{d}\Omega - \delta t \oint_{\partial\Omega} (\mathbf{f}(\hat{\mathbf{u}})\mathbf{n} - \breve{p}\mathbf{n})\,\mathrm{d}s = \mathbf{0}. \tag{10}$$

The auxiliary velocity $\breve{\mathbf{u}}$ does not satisfy the incompressibility constraint (2). Therefore, we correct the auxiliary velocity (in the second step) by adding the thus far neglected part of the pressure, i.e. $\mathbf{u}^{n+1}$ is solved from

$$\int_\Omega (\alpha+\tfrac{1}{2})(\mathbf{u}^{n+1} - \breve{\mathbf{u}})\,\mathrm{d}\Omega + \delta t \oint_{\partial\Omega} q\,\mathbf{n}\,\mathrm{d}s = \mathbf{0}, \tag{11}$$

where (first) the pressure correction $q = \hat{p} - \breve{p}$ is determined such that (4) holds.

4. A fourth-order finite-volume method

We will construct a fourth-order finite-volume method as the Richardson extrapolate of a well-known second-order method. To make this paper self-contained, we will summarize the main lines of the second-order spatial discretization (in Section 4.1) before discussing its fourth-order Richardson extrapolate (in Section 4.1). The treatment of the boundaries, the implementation of the incompressibility constraint, and the discretization on (weakly) stretched grids will be discussed in Sections 4.3, 4.4 and 4.5, respectively.

In order to present the mathematical expressions conveniently, we will restrict ourselves to two spatial dimensions in this section; the extension to 3D is straightforward.

4.1. A SECOND-ORDER FINITE-VOLUME METHOD

The flow domain is covered by an orthogonal grid. To start with, we will consider uniform grids; (weakly) stretched grids will be considered in Section 4.5. The velocity and pressure are defined on the grid as proposed by Harlow and Welsh [12].

The time-discrete momentum equation (10) is applied to control volumes. The definition of the control volumes is illustrated in Figure 2. The lower right-hand shaded rectangle shows a control volume for the horizontal component of (10). The upper left-hand shaded rectangle depicts a control volume for the vertical component.

All spatial integrations (over the control volumes as well as over their surfaces) are approximated by means of the midpoint rule, with linear interpolations for the convective flux and

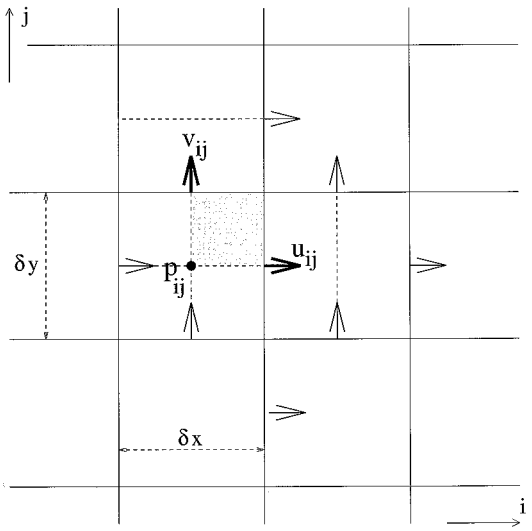

Figure 2. The staggered locations of the discrete velocity and pressure and the definition of the control volumes.

central differences for the diffusive flux. The central spatial discretization method gives

$$(\breve{u}_{ij} - u^n_{ij})\delta x\delta y = \delta t(f_{i+1/2,j} - f_{i-1/2,j})\delta y + \delta t(f_{i,j+1/2} - f_{i,j-1/2})\delta x - \delta t(\breve{p}_{i+1,j} - \breve{p}_{i,j})\delta y, \tag{12}$$

$$(\breve{v}_{ij} - v^n_{ij})\delta x\delta y = \delta t(g_{i+1/2,j} - g_{i-1/2,j})\delta y + \delta t(g_{i,j+1/2} - g_{i,j-1/2})\delta x - \delta t(\breve{p}_{i,j+1} - \breve{p}_{i,j})\delta x, \tag{13}$$

where

$$f_{i+1/2,j} = -\tfrac{1}{4}(\hat{u}_{i+1,j} + \hat{u}_{i,j})^2 + \frac{1}{\mathrm{Re}}\frac{1}{\delta x}(\hat{u}_{i+1,j} - \hat{u}_{i,j}),$$

$$f_{i,j+1/2} = -\tfrac{1}{4}(\hat{v}_{i+1,j} + \hat{v}_{i,j})(\hat{u}_{i,j+1} + \hat{u}_{i,j}) + \frac{1}{\mathrm{Re}}\frac{1}{\delta y}(\hat{u}_{i,j+1} - \hat{u}_{i,j}),$$

$$g_{i+1/2,j} = -\tfrac{1}{4}(\hat{u}_{i,j+1} + \hat{u}_{i,j})(\hat{v}_{i+1,j} + \hat{v}_{i,j}) + \frac{1}{\mathrm{Re}}\frac{1}{\delta x}(\hat{v}_{i+1,j} - \hat{v}_{i,j}),$$

$$g_{i,j+1/2} = -\tfrac{1}{4}(\hat{v}_{i,j+1} + \hat{v}_{i,j})^2 + \frac{1}{\mathrm{Re}}\frac{1}{\delta y}(\hat{v}_{i,j+1} - \hat{v}_{i,j}).$$

The auxiliary velocity $(\breve{u}_{i,j}, \breve{v}_{i,j})$ is corrected such that Equation (4) holds for control volumes that are centred on the pressure. Once more, the midpoint rule is applied to approximate the integrals numerically. This leads to a discrete Poisson equation for the pressure correction.

4.2. The fourth-order Richardson extrapolate

The leading term of the truncation error of the approximation (12)–(13) consists of second-order terms. The terms next in size are of order four. Hence, elimination of the leading term results in a fourth-order method.

To eliminate the leading term of the truncation error of the second-order method, the momentum equations are also integrated over control volumes that are three times larger. Figure 3 (right) illustrates the definition of such a larger control volume for the horizontal component of the momentum equation. The definition of a control volume for the vertical component is obtained by a rotation of Figure 3 one quarter of a turn in a counter-clockwise direction.

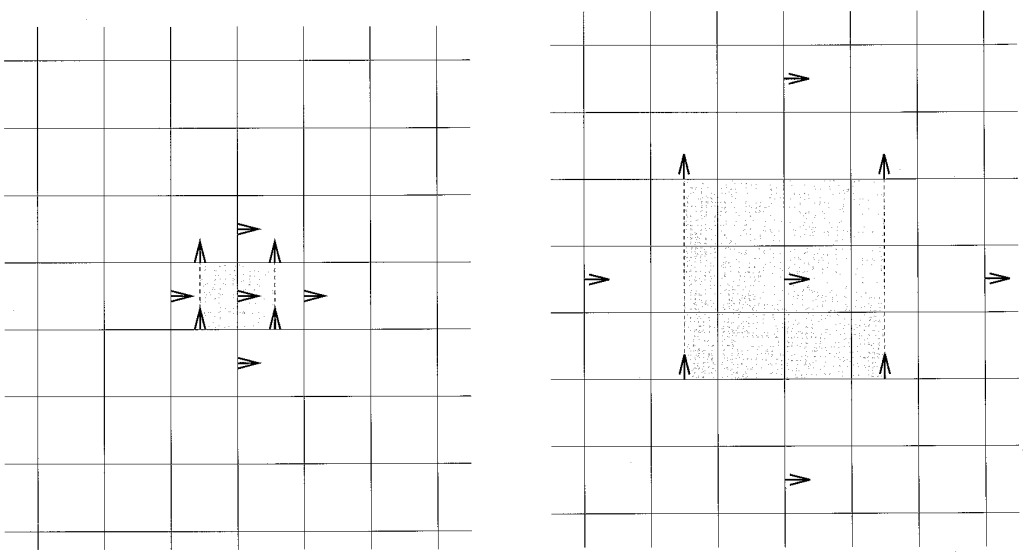

Figure 3. The left picture shows a control volume for the conservation of the horizontal component of the momentum field (in two spatial dimensions). The right picture shows a three-times larger control volume that is applied to eliminate the leading term of the truncation error. The arrows denote the components of the discrete velocity that are used to discretize the application of the conservation law to the control volume.

The larger control volumes are chosen in such a way that their corners coincide with positions of the vertical velocity. Three times larger volumes are the smallest ones possible with corners at these positions. The coinciding of corners with vertical velocities implies that one discretization method can be used for the spatial integration of equation (10) over both the original control volumes and the larger volumes. Two times larger control volumes, for instance, have corners that do not coincide with positions of the vertical velocity, and thus, do require additional high-order interpolations (e.g. for the cross terms in the convective flux).

The discrete conservation law for the original control volume is expressed in terms of nearby velocities: for the horizontal component in terms of five nearby horizontal velocities and four nearby vertical velocities; see Figure 3 (left). The same interpolation, differentiation and integration rules are applied to the three times larger control volume. Hence, the truncation error in the integration of the momentum equations over the three times larger control volume is of the same form as the truncation error in the integration over the original control volume. We denote the auxiliary velocity that results from the integration of (10) over the three times larger control volumes by $(\breve{U}, \breve{V})$

$$(\breve{U}_{ij} - u^n_{ij})3\delta x 3\delta y \;=\; \delta t(F_{i+3/2,j} - F_{i-3/2,j})3\delta y + \delta t(F_{i,j+3/2} - F_{i,j-3/2})3\delta x$$
$$-\delta t(\breve{p}_{i+2,j} - \breve{p}_{i-1,j})3\delta y, \qquad (14)$$

$$(\breve{V}_{ij} - v^n_{ij})3\delta x 3\delta y = \delta t(G_{i+3/2,j} - G_{i-3/2,j})3\delta y + \delta t(G_{i,j+3/2} - G_{i,j-3/2})3\delta x$$
$$-\delta t(\breve{p}_{i,j+2} - \breve{p}_{i,j-1})3\delta x, \tag{15}$$

where

$$F_{i+3/2,j} = -\tfrac{1}{4}(\hat{u}_{i+3,j} + \hat{u}_{i,j})^2 + \frac{1}{\mathrm{Re}}\frac{1}{3\delta x}(\hat{u}_{i+3,j} - \hat{u}_{i,j}),$$

$$F_{i,j+3/2} = -\tfrac{1}{4}(\hat{v}_{i+2,j+1} + \hat{v}_{i-1,j+1})(\hat{u}_{i,j+3} + \hat{u}_{i,j}) + \frac{1}{\mathrm{Re}}\frac{1}{3\delta y}(\hat{u}_{i,j+3} - \hat{u}_{i,j}),$$

$$G_{i+3/2,j} = -\tfrac{1}{4}(\hat{u}_{i+1,j+2} + \hat{u}_{i+1,j-1})(\hat{v}_{i+3,j} + \hat{v}_{i,j}) + \frac{1}{\mathrm{Re}}\frac{1}{3\delta x}(\hat{v}_{i+3,j} - \hat{v}_{i,j}),$$

$$G_{i,j+3/2} = -\tfrac{1}{4}(\hat{v}_{i,j+3} + \hat{v}_{i,j})^2 + \frac{1}{\mathrm{Re}}\frac{1}{3\delta y}(\hat{v}_{i,j+3} - \hat{v}_{i,j}).$$

The truncation error in the approximation of $(\breve{U}, \breve{V})$ is of the same form as the truncation error in the approximation of $(\breve{u}, \breve{v})$. On a uniform grid, the leading term of the truncation error in the approximation of the conservation law to a three times larger volume is precisely nine times as large as the leading term of the approximation to a corresponding original volume. Thus, subtracting $\frac{1}{8}$ times the result of the integration of the conservation law over the large control volume from $\frac{9}{8}$ times the result of the second-order integration (i.e. taking $\frac{9}{8}\breve{u} - \frac{1}{8}\breve{U}$ and $\frac{9}{8}\breve{v} - \frac{1}{8}\breve{V}$) we may eliminate the second-order terms of the truncation error and obtain a fourth-order accurate spatial discretization of the time-discrete momentum equation (10).

4.3. Treatment of the boundaries

In the vicinity of boundaries, some three times larger control volumes do not fit into the flow domain. A misfit is treated separately: here, the leading term in the truncation error of the numerical integration of fluxes through some parts of the boundary of a control volume is not eliminated, i.e. the second-order finite-volume discretization is used for misfitting parts.

This approach is similar to the one that is followed in most of the higher-order methods that are mentioned in Section 1. The large high-order-accurate stencils used by, for instance, [3], [4] and [6] can also not be applied near boundaries, since there is not enough space avaliable to do so, and no attempt has been made to discretize with a high-order of accuracy in the neighborhood of boundaries: in that neighborhood the order of the approximation is simply reduced, depending on the available number of grid points.

4.4. Implementation of the incompressibility constraint

We update the velocity by integrating the momentum equations over one time step and by correcting the result by adding the pressure correction in such a way that the mass is conserved in control volumes centred on the pressures. Obviously, we can also apply the balance of mass to three times larger control volumes and use these control volumes to eliminate the leading term in the truncation error. Thus, a fourth-order-accurate spatial discretization of equation (4) can be derived.

Here, we do not follow that approach: we simply use the same control volumes as in a second-order finite-volume method. That is, the approximation of the Laplacian in the Poisson equation for the pressure correction q is second-order accurate, and not fourth-order. It may be noted that the pressure correction q is of the order of δt^2. Indeed, by definition, $q = \hat{p} - \breve{p}$, and both $\hat{p}$ and $\breve{p}$ are second-order accurate approximations of $p^{n+\alpha}$; see Section 3.2. So, even with a second-order accurate spatial discretization the overall error is of the order four: $O(\delta x^2 \delta t^2, \delta y^2 \delta t^2)$.

4.5. WHAT ABOUT STRETCHED GRIDS?

We restrict ourselves to weakly stretched grids, i.e. adjacent cells differ hardly in size. On such grids the fourth-order finite-volume discretization is to be modified somewhat.

Figure 2 shows a control volume that is centred around u_{ij}. The corners of this control volume coincide with positions of the vertical velocity v, i.e. the v-points define the control volumes around the u's. This holds both for uniform grids and for stretched grids. Likewise, the corners of a control volume around the v's coincide with u-points.

We approximate a diffusive flux through a surface of a control volume by the difference of the nearest velocity at the left and the nearest velocity at the right of the surface divided by the product of the distance between the locations of these two velocities and the Reynolds number. Formally, this discretization is not second-order accurate, since the surface of the control volume does not lie midway. Yet, for weakly stretched grids the surface is only slightly off-centre, and the discretization is sufficiently accurate.

To evaluate the convective flux through a surface of a control volume, the velocities are interpolated first. We compute the approximation of the term u^2 in $f_{i\pm 1/2,j}$ by squaring the result of the linear interpolation of u at the surface $i \pm 1/2$. The term v^2 in $g_{i,j\pm 1/2}$ is approximated likewise. The cross-terms in $f_{i,j\pm 1/2}$ and $g_{i\pm 1/2,j}$ are also approximated by products of interpolated velocities. The product of u and v at the point of intersection of the horizontal grid line through $v_{i,j}$ and the vertical grid line through $u_{i,j}$, for instance, is approximated by the product of a linear interpolation of $u_{i,j+1}$ and $u_{i,j}$ and a linear interpolation of $v_{i,j}$ and $v_{i,j+1}$ (these four velocity components are indicated in Figure 2).

For a conservative discretization the flux through a surface has to be computed independent of the control volume in which it is considered. Two adjacent control volumes see one flux through their common surface; one sees it as an ingoing flux, the other sees it as an outgoing flux. This fundamental property is lost if the weights in the Richardson extrapolation depend on control volumes. Therefore, we use the weights $\frac{9}{8}$ and $-\frac{1}{8}$ also for weakly stretched grids. Finally, it may be noted that, for constant weights, the matrix that represents the discretization of a second-order derivative is symmetric; the discretization of a first-order derivative is anti-symmetric. The favourable influence of this property of the coefficient matrix on the global discretization error has been stressed already by Veldman and Rinzema [13].

5. A comparison of the second- and the fourth-order method

5.1. EXPERIMENTAL DATA

The experimental data of the flow in a cubical lid-driven cavity at $\mathrm{Re} = 10,000$ in [14] consists of mean velocities and turbulence intensities along two centerlines in the plane of symmetry. Figure 4 illustrates the locations of the measurements in the cavity. The velocity measurements have been performed with an optical laser-Doppler anemometer system. The

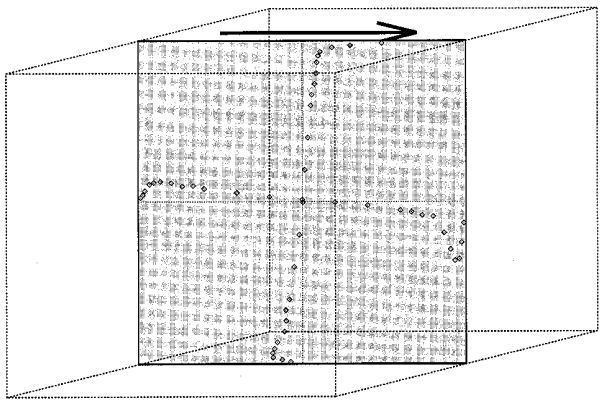

Figure 4. Locations of the measurements. The orientation of the cavity is such that the upper-plane is driven from the left to the right.

speed at which the upper-lid of the cavity is driven is 0·0666 m/s. The overall error in an instantaneously measured velocity is about $\pm 0{\cdot}0004$ m/s, i.e. 0·6% of the maximum velocity. The physical length, height and depth of the cavity are 0·15 m. Up to 5·46 minutes of velocity data has been accumulated at each measuring point. This period, 5·46 minutes, corresponds to approximately 145 units of the time scale $0{\cdot}15/0{\cdot}0666$.

5.2. SECOND-ORDER RESULTS

In [15], we have shown that the outcomes of a direct numerical simulation using a second-order finite-volume technique and a 100^3 grid, agree well with the experimental data. This holds for all the quantities that have been measured.

5.3. CHEAPER AND BETTER: RESULTS OF THE FOURTH-ORDER METHOD

Recently, we have re-done the DNS of a turbulent flow in a driven cavity at $\mathrm{Re} = 10^4$ with the fourth-order method using various grids. It turned out that one Richardson extrapolation improves the results significantly.

For example, on a stretched 50^3 grid (the gridspacing is geometrically stretched away from the wall; the largest mesh width is approximately seven times wider than the smallest), the agreement between the mean velocities and turbulence intensities obtained with the fourth-order method and the experiments is better than the agreement between the results of the second-order method on a 100^3 grid and the experiments. To illustrate this, mean velocities as obtained from the second-order DNS, the fourth-order DNS and from the experiment are compared in Figure 5.

In this example the fourth-order results are clearly superior to the second-order results, whereas the computational effort is about twenty times less. Indeed, the CPU-time per grid point and time step of both methods is comparable, a 50^3 grid has 8 times less grid points than a 100^3 grid, it allows for a twice as large a time step (note that the time step is restricted by the CFL-condition), and the number of iterations needed to solve the pressure correction from the Poisson equation is somewhat less for a 50^3 grid than for a 100^3 grid: $8 \times 2 \times 1{\cdot}25 = 20$.

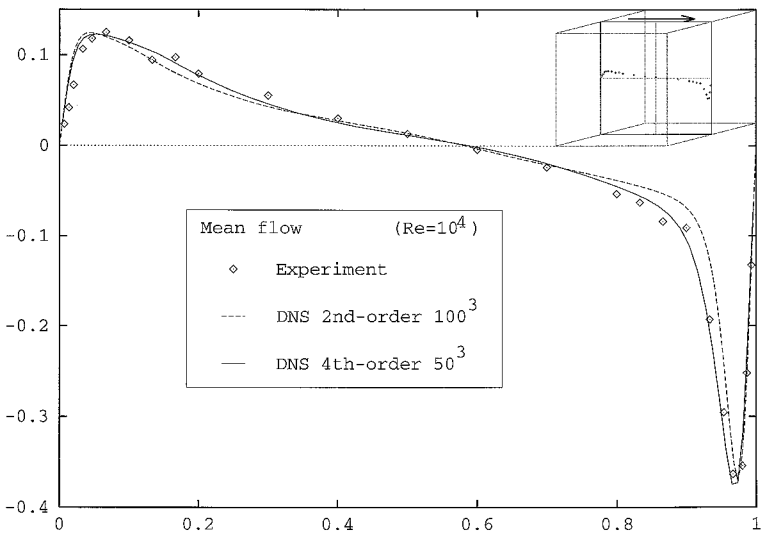

Figure 5. Second- and fourth-order DNS vs. experiment in a 3D driven cavity at Re $= 10,000$. Shown is the vertical mean velocity on the horizontal centerline in the symmetry plane of the cavity.

6. Flow in a driven cavity at Re = 50,000

As is shown in Section 5.3, the fourth-order simulation technique is more economical than the second-order method. Thus, with the fourth-order method higher Reynolds numbers can be tackled. On a 192^3 grid a DNS of a turbulent flow in a driven cavity at Re $= 50,000$ is feasable. Results of this DNS are presented in Section 6.2. In addition, mean velocities and power spectra at Re $= 50,000$ are compared with their equivalents at Re $= 10,000$. First, some details of the simulation are described.

6.1. Details of the simulation

All lengths are made dimensionless with the height of the cavity taken as unit length; velocities are made dimensionless with the help of the speed at which the lid is driven. The cubical cavity is represented by a 192^3 grid. No-slip conditions are imposed at all walls. The grid is stretched away from the walls; the smallest grid size is $2{\cdot}5\,10^{-3}$; the largest is approximately five times larger. The time step equals 0·001. After the flow has reached its statistical equilibrium, 175 (dimensionless) time units have been computed. This period corresponds to about 35 large-eddy turn-around times. Statistics have been sampled every time step.

The discrete Poisson equation for the pressure correction is solved by means of the conjugate gradient method with modified incomplete Choleski preconditioning. The preconditioner is modified according to Gustafson (see e.g. [16]; the parameter, called ξ in [16], is set to 10). The MICCG code is fully vectorized by an explicit reordering of the unknowns along diagonals of grid planes parallel to the symmetry plane of the cavity. The implementation of the preconditioned iterative method is optimized as proposed by Eisenstat [17]. The initial guess for the iteration is obtained by extrapolation of the pressure correction from previous time levels.

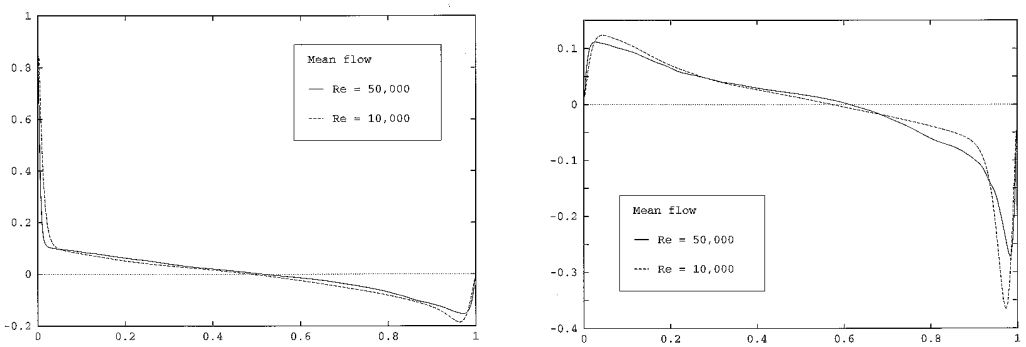

Figure 6. Comparison of mean velocities in the central plane of the cavity at Re $= 10,000$ and Re $= 50,000$. The continuous line corresponds to Re $= 50,000$; the dashed line corresponds to Re $= 10,000$. The left picture shows the horizontal velocity along the vertical centre line; the right picture shows the vertical velocity along the horizontal centre line.

Table 1. Maximum values of $\overline{v'v'}$ and $\overline{u'v'}$ along the horizontal centre line in the central plane. Here u' denotes the horizontal component of the fluctuating velocity; v' is the vertical component.

Reynolds number	$\overline{v'v'}$		$\overline{u'v'}$	
	peak	location	peak	location
10,000	0·104	0·957	$1{\cdot}11\ 10^{-3}$	0·952
50,000	0·146	0·983	$1{\cdot}63\ 10^{-3}$	0·956

6.2. RESULTS

In this section some results of the fourth-order method at Re $= 50,000$ are presented. Mean velocities, turbulence intensities and power spectra are computed and compared to their equivalents at Re $= 10,000$. Mean velocities along the centre lines in the central plane are compared in Figure 6. It may be noted that the velocities have been averaged over a relatively short period of time, namely over 35 large-eddy turn-around times. Table 1 shows the peak values (and their locations) of turbulence intensities along the horizontal centre line in the central plane at Re $= 10,000$ and Re $= 50,000$. As can be seen from Table 1, the maximum of $\overline{v'v'}$ lies approximately two and a half times closer to the wall at Re $= 50,000$ than at Re $= 10,000$. It may be remarked that at Re $= 50,000$ the maximum of $\overline{v'v'}$ is reached at the sixth grid point as counted from the wall.

Unfiltered power spectra of a horizontal velocity near the bottom of the cavity are compared in Figure 7. In both spectra a $-\frac{5}{3}$ slope can be observed.

Figure 8 shows a snapshot of the vorticity in the central plane of the cavity at Re $= 50,000$. Compared to the flow at Re $= 10,000$ the number of small-scale vortical structures has increased drastically. To verify that all these small structures are indeed resolved, we have estimated the Taylor micro-scale from the flow data by approximating the distance

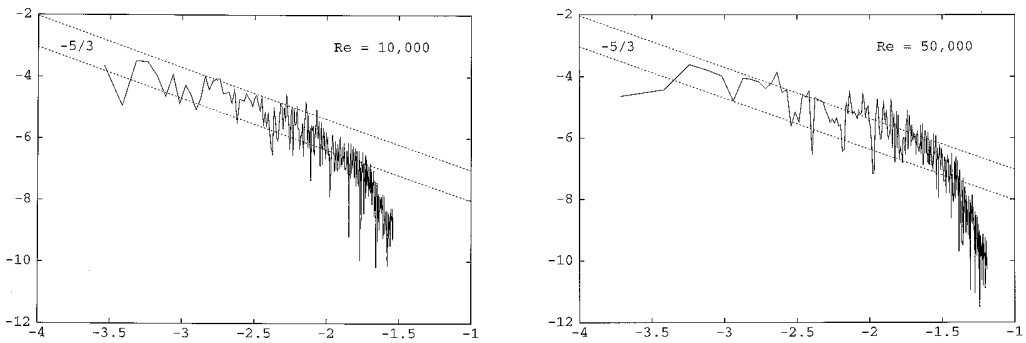

Figure 7. Comparison of power spectra at Re $= 10,000$ (left) and Re $= 50,000$ (right). Both pictures show the power spectrum of a *u*-velocity at a point at 2% of the height of the cavity along the vertical centre line in the central plane of the cavity (log-log plot).

between the location of the maximum and that of the zero of the osculating parabola of a computed two-point velocity auto-correlation: the number of grid points per Taylor micro-scale is approximately equal to 8.

7. Flow past a square cylinder at Re = 22,000

In this section we consider the flow past a square cylinder at Re $= 22,000$ (at zero angle of attack). This flow served as a test case for two LES workshops. Experimental data is available for comparison. A summary of the results presented at these workshops can be found in [8] and [9].

Also for the flow past a square cylinder at Re $= 22,000$, the fourth-order method performs better than the second-order method. On a $280 \times 210 \times 64$ grid all our second-order simulations crashed (due to insufficient spatial resolution), while the fourth-order simulation method performed well.

7.1. Details of the simulation

The coordinate system has its origin at the centre of the cylinder. All quantities are normalized by the cylinder width and the inflow velocity. The stream-wise direction is denoted by x, the lateral direction by y and the spanwise (periodical) direction by z. The components of the velocity in these directions are given by u, v and w, respectively.

The inflow boundary is located at $x = -7$, i.e. six and a half diameters upstream of the cylinder. The inflow condition reads $u = 1, v = 0, w = 0$. The lateral boundaries are located at $y = \pm 7$. At these boundaries we have imposed $u_{yy} = w_{yy} = p_y = 0$, where p is the pressure. The outflow boundary is located at $x = 20$. The outflow conditions read $v_{xx} = w_{xx} = 0$ and $p_x =$ constant, where the constant is determined such that the mass inflow equals the mass outflow (at each time step); this constant is approximately zero. In addition, in a buffer zone $(x = 15 - 20)$ the Reynolds number is decreased from 22,000 to 1,000 to suppress (non-physical) waves which are reflected by the artificial outflow boundary. The spanwise boundaries are four diameters apart. No-slip boundaries are imposed at the cylinder surface.

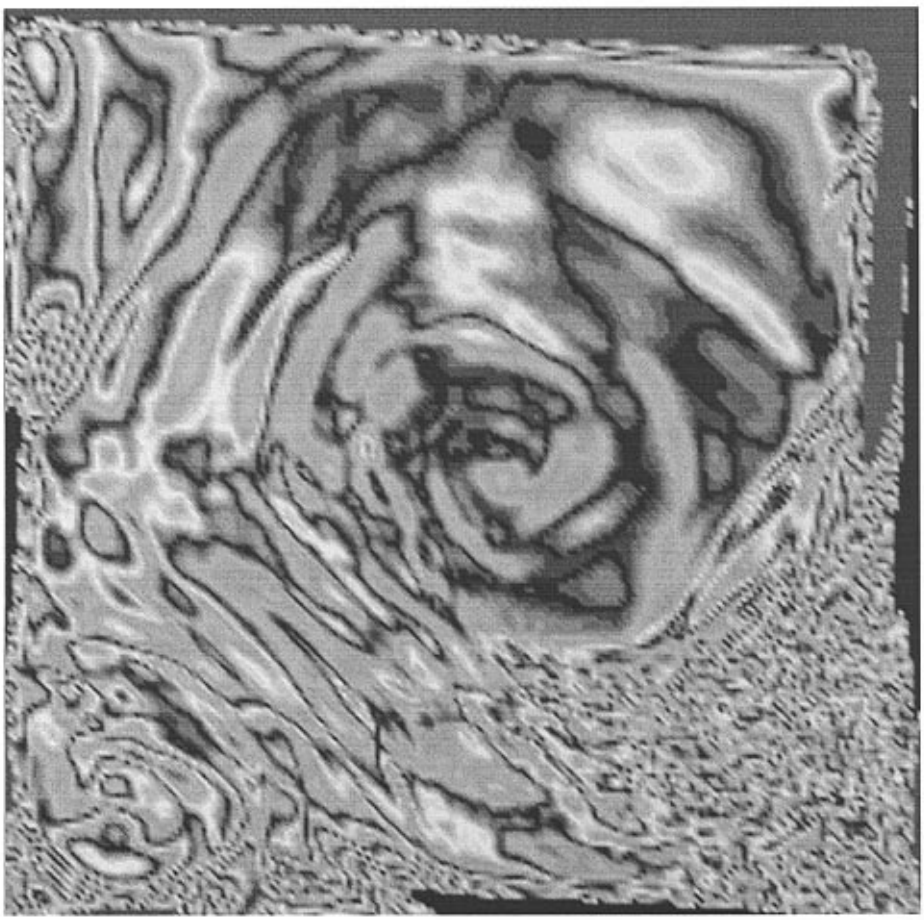

Figure 8. An illustration of the structures in the central plane of the cavity at $\mathrm{Re} = 50,000$. The orientation of the cavity is such that the upper lid is driven from the left to the right. Shown is the third component of the vorticity vector in the central plane of the cavity. Here, the vorticity is averaged over one large-eddy turn-around time.

We have used a $280 \times 210 \times 64$ (stretched and staggered) grid to cover the computational domain. The first grid point is spaced 0·005 from the cylinder surface. The grid is stretched out away from the cylinder surface by means of a sinh function; the ratio of the largest to smallest grid size is approximately 200 (in x) and 100 (in y). It may be emphasized that we have not adapted the weights in the Richardson extrapolation to the stretching of the grid. As explained in Section 4.5, we always use the constant weights $\frac{9}{8}$ and $-\frac{1}{8}$, since these weights result in a conservative discretization. The time step equals 0·001. Statistics are sampled at each time step.

The discrete Poisson equation for the pressure is solved with a combination of a Fast Fourier Transform method in the spanwise direction and a Modified Incomplete Choleski Conjugate Gradient method in the resulting spectral space. After the Fourier transform (which can be computed in parallel over the x and y directions), the discrete Poisson equation falls apart into a set of mutually independent 2D Klein–Gordon–Fokker equations. This set of mutually independent equations is distributed over the processors, and solved. Thus, a fully parallel implementation is achieved. More details can be found in [18].

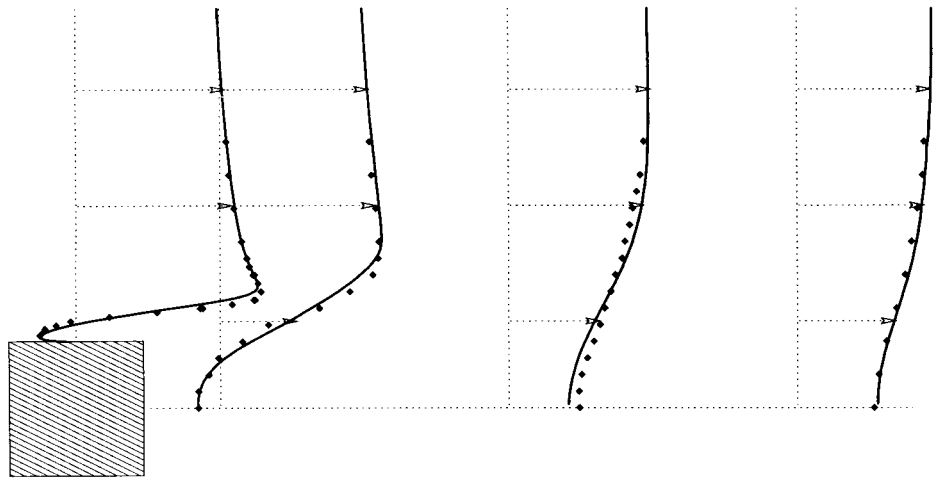

Figure 9. A comparison of mean velocities of the DNS with experimental results. The experimental data is taken from ERCOFTAC Database Case 43; see also Lyn et al. [19]. Shown is the mean stream-wise velocity. The continuous lines correspond to the DNS; the experimental data is depicted by the dots.

Table 2. Comparison of DNS with experiment

	DNS	Experiments		
		Lyn et al. [19]	McLean et al. [20]	Lee [21]
Mean Strouhal number	0·133	0·133 ± 0·003	—	—
Mean drag coefficient Cd	2·09	2·1	1·9–2·1	2·05
Mean lift coefficient Cl	0·005	—	—	—
Rms fluctuation of Cd	0·178	—	0·1–0·2	0·16–0·23
Rms fluctuation of Cl	1·45	—	0·7–1·4	—

7.2. PREDICTED DATA

The start-up of the flow plus three shedding cycles have been computed. Averages are computed over three shedding cycles and the spanwise direction. Velocities are also averaged over the top and bottom halves. Table 2 shows the mean Strouhal number, the mean drag coefficient Cd, the mean lift coefficient Cl and the root-mean-square fluctuations of Cd and Cl.

It may be noted that the mean lift coefficient has not been measured; it should be zero. So far, we have only computed three full shedding cycles. Yet, the computed values of all bulk quantities fall within the range set by the experiments, except for the root-mean-square of the fluctuations of the lift coefficient Cl. The rms fluctuation of Cl seems to be slightly overestimated by the DNS.

Figure 9 shows the mean stream-wise velocity at four locations past the cylinder.

8. Conclusion

The impetus of improvements in numerical algorithms (in particular space discretization and time-integration) on turbulent-flow simulation has been adressed. It has been demonstrated

that the algorithmic improvements, together with the improvements in computer performance, have opened the possibility of performing DNS in the Reynolds number range $10^4 - 10^5$.

Acknowledgements

The Stichting Nationale Computerfaciliteiten (National Computing Facilities Foundation, NCF) with financial support from the Netherlands Organization for Scientific Research (NWO) is gratefully acknowledged for the use of supercomputer facilities.

References

1. E. Hairer and G. Wanner, *Solving Ordinary Differential Equations II*. Berlin: Springer-Verlag (1991) 601pp.
2. H. Le and P. Moin, An improvement of fractional step methods for the incompressible Navier–Stokes equations. *J. Comp. Phys.* 92 (1991) 367–379.
3. M. M. Rai and P. Moin, Direct simulations of turbulent flow using finite-difference schemes. *J. Comp. Phys.* 96 (1991) 15–53.
4. H. F. Fasel, Numerical simulation of instability and transition in boundary layer flows. In: D. Arnal and R. Michel (eds.), *Laminar-Turbulent Transition*. Berlin: Springer-Verlag (1990) pp. 303–308.
5. R. D. Joslin, C. L. Streett and C. L. Chang, Validation of three-dimensional incompressible spatial direct numerical simulation code – a comparison with linear theory and parabolic stability equation theories for boundary layer transition on a flat plate, NASA Technical Paper 3205 (1992) 18pp.
6. Z. Liu and C. Liu, Fourth order finite difference and multigrid methods for modeling instabilities in flat plate boundary layers – 2D and 3D approaches, *Computers & Fluids* 7 (1994) 955–982.
7. A. G. Kravchenko, P. Moin and R. Moser, Zonal embedded grids for numerical simulation of wall-bounded turbulent flows. *J. Comp. Phys.* 127 (1996) 412–423.
8. W. Rodi, J. H. Ferziger, M. Breuer and M. Pourquié, Status of Large Eddy Simulation: Results of a workshop. To appear in *ASME J. Fluids Eng.* (1996).
9. P. R. Voke, Flow past a square cylinder: test case LES2. To appear in: J. P. Chollet et al. (eds.), *Direct and Large Eddy Simulation II* (1997).
10. R. W. C. P. Verstappen, J. G. Wissink and A. E. P. Veldman, Direct numerical simulation of driven cavity flows, *Appl. Sci. Res.* 51 (1993) 377-381.
11. O. Nevanlinna and W. Liniger, Contractive methods for stiff differential equations; Part I. *BIT* 18 (1978) 457–474.
12. F. H. Harlow and J. E. Welsh, Numerical calculation of time-dependent viscous incompressible flow of fluid with free surface. *Phys. Fluids* 8 (1965) 2182–2189.
13. A. E. P. Veldman and K. Rinzema, Playing with nonuniform grids. *J. Eng. Math.* 26 (1992) 119-130.
14. A. K. Prasad and J. R. Koseff, Reynolds number and end-wall effects on a lid-driven cavity flow. *Physics of Fluids A* 1 (1989) 208–218.
15. R. W. C. P. Verstappen and A. E. P. Veldman, Direct numerical simulation of a 3D turbulent flow in a driven cavity at Re $= 10,000$. In: Wagner et al. (eds.), *Computational Fluid Dynamics '94*. Chichester: John Wiley & Sons (1994) 558–565.
16. I. Gustavson, A class of first order factorization methods. *BIT* 18 (1978) 142–156.
17. S. C. Eisenstat, Efficient implementation of a class of preconditioned Conjugate Gradient methods, *SIAM J. on Scientif. and Stats. Comp.* 2 (1981) 1–4.
18. R. W. C. P. Verstappen and A. E. P. Veldman, Data-parallel solution of the incompressible Navier-Stokes equations. In: P. Wesseling (ed.), *High Performance Computing in Fluid Dynamics*. Dordrecht: Kluwer Academic Publishers (1996) pp. 237–260.
19. D. A. Lyn, S. Einav, W. Rodi and J. H. Park, A laser-Doppler-velocimetry study of emsemble-averaged characteristics of the turbulent near wake of a square cylinder. *J. Fluid Mech.* 304 (1995) 285–316.
20. I. McLean and I. Gartshore, Spanwise correlations of pressure on a rigid square section cylinder. *J. Wind Eng.* 779 (1992) 41–44.
21. B. E. Lee, The effect of turbulence on the surface pressure field of square prisms. *J. Fluid Mech.* 69 (1975) 263–282.